Journal of Nuclear Materials 393 (2009) 126–133

Contents lists available at ScienceDirect

Journal of Nuclear Materials

journal homepage: www.elsevier.com/locate/jnucmat

10 MeV Au ion irradiation effects in an MgO–HfO_2 ceramic–ceramic (CERCER) composite

J.A. Valdez *, I.O. Usov, J. Won, M. Tang, R.M. Dickerson, G.D. Jarvinen, K.E. Sickafus

Los Alamos National Laboratory, Los Alamos, NM 87545, USA

ARTICLE INFO

Article history:
Received 24 March 2009
Accepted 26 May 2009

PACS:
61.80.Jh
68.55.aj
81.05.Kf
81.40.Wx

ABSTRACT

Room temperature ion irradiation damage studies were performed on a ceramic composite intended to emulate a dispersion nuclear fuel. The composite is composed of 90-mole% MgO and 10-mole% HfO_2. The as-synthesized composite was found to consist of $Mg_2Hf_5O_{12}$ (and some residual HfO_2) particles embedded in an MgO matrix. X-ray diffraction revealed that nearly all of the initial HfO_2 reacted with some MgO to form $Mg_2Hf_5O_{12}$. Ion irradiations were performed using 10 MeV Au^{3+} ions at room temperature over a fluence range of 5×10^{16}–5×10^{20} Au/m^2. Irradiated samples were characterized using both grazing incidence X-ray diffraction (GIXRD) and transmission electron microscopy (TEM), the latter using both selected-area electron diffraction (SAED) and micro-diffraction (μD) on samples prepared in cross-sectional geometry. Both GIXRD and TEM electron diffraction measurements on a specimen irradiated to a fluence of 5×10^{20} Au/cm^2, revealed that the initial rhombohedral $Mg_2Hf_5O_{12}$ phase was transformed into a cubic-$Mg_2Hf_5O_{12}$ phase. Finally, it is important to note that at the highest ion fluence used in this investigation (5×10^{20} Au/m^2), both the MgO matrix and the $Mg_2Hf_5O_{12}$ second phase remained crystalline.

Published by Elsevier B.V.

1. Introduction

For over a half-century, nuclear energy programs have struggled to safely dispose of spent nuclear fuel (SNF). The new global focus is on reducing the radiotoxicity and health risks of SNF by using reprocessing technologies. This focus has spawned a DOE research program called the Advanced Fuel Cycle Initiative (AFCI), to develop a closed nuclear fuel cycle by transmuting major SNF radiotoxic constituents in nuclear reactors or efficiently packaging them for disposal. The final waste in this closed-cycle concept is far more benign than SNF. In conjunction with AFCI, radiation effects in crystalline oxide ceramics (for example UO_2, ZrO_2, MgO and $MgAl_2O_4$) have been the focus of recent investigations, mainly due to their excellent radiation stability and their potential as nuclear waste or fuel forms [1–10]. The study presented here focuses on ion irradiation effects in a two-phase oxide ceramic, a ceramic–ceramic (CERCER) composite intended to simulate a dispersion nuclear fuel with the following properties: (i) the minority phase is designed to accommodate fissile species such as uranium and higher actinides; (ii) the majority (matrix) phase is inert (non-fissile), but designed to retain fission products (FPs) produced by actinide burnup; (iii) the composite is designed to maintain structural integrity while exposed to high radiation fields; and (iv) the inert matrix phase is designed to be chemically-separable from the actinide-bearing minority phase (in a dissolution process). The latter property is intended to promote easy separation of FPs and actinides during reprocessing. In this fuel design FPs originate from within the actinide-bearing, kernel particles with high kinetic energies (up to ~100 MeV) and travel several microns in the composite. If the size of the kernel particles is less than the FP range, and the kernel particles are spaced appropriately, then the majority of FPs will come to rest in the matrix phase. Thus, a natural partitioning evolves between the actinides and FPs during the burning cycle of the fuel. By choosing a matrix material that can be selectively chemically dissolved, a process can be developed to separate actinides from FPs in the spent fuel and to recover FPs from the host matrix. This separation strategy has the potential to greatly reduce technological challenges associated with conventional spent fuel reprocessing procedures. As a surrogate for a dispersion nuclear fuel, the CERCER composite that we examined in this preliminary study consists of small $Mg_2Hf_5O_{12}$ particles dispersed in an MgO host matrix. We present here preliminary results regarding the synthesis and fabrication of this composite, as well as the response of this composite to energetic ion irradiation.

2. Experimental details

CERCER composite samples were synthesized from MgO (Alpha Aesar, Puratronic, 99.998% (metals basis)) and HfO_2 (Alpha

* Corresponding author. Address: Los Alamos National Laboratory, Materials Science and Technology Division, Mail-Stop G755, Los Alamos, NM 87545, USA. Tel.: +1 505 665 3034; fax: +1 505 667 8601.
E-mail address: javaldez@lanl.gov (J.A. Valdez).

0022-3115/$ - see front matter Published by Elsevier B.V.
doi:10.1016/j.jnucmat.2009.05.019

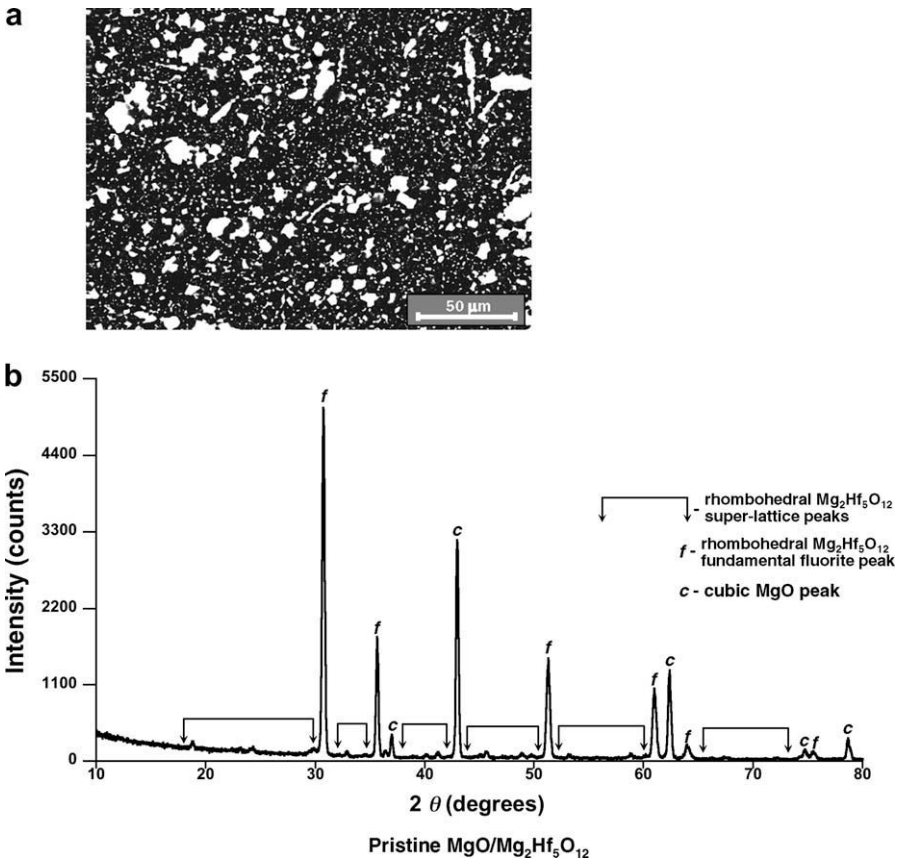

Fig. 1. (a) Scanning electron microscope image (collected in backscatter mode) obtained from a polished pellet of a 90MgO:10HfO_2 composite specimen. Dark regions in the image are MgO whereas the bright regions are $Mg_2Hf_5O_{12}$ second phase particles. This image shows a fairly uniform bimodal distribution of $Mg_2Hf_5O_{12}$ particles in the MgO matrix phase. (b) X-ray diffraction pattern obtained from a polished pristine 90MgO/10HfO_2 composite pellet. Peak indexing revealed that the pellet is composed primarily of two major phases: cubic-MgO and rhombohedral-$Mg_2Hf_5O_{12}$.

Aesar, 99.99%, metals basis excluding Zr, Zr <100 ppm) powders. These end-member oxide powders were calcined at 1000 °C for 24 h, then weighed to a starting chemistry of 9:1 mol% Mg:Hf ratio. MgO/HfO_2 powders were ball-milled in a Spex Certiprep 8100 high-energy mill (5 g at a time) for 2 h in a Si_3N_4 vial with two Si_3N_4 balls and 1 ml of Hexane (to prevent agglomeration). Ball-milled powders were cold-pressed using a pressure of 400 MPa in a 13 mm diameter stainless steel die. After pressing, the pellets were heat treated in a platinum crucible at 1600 °C in air for 24 h, then quenched to room temperature by removing the crucible from the furnace and placing it on a chilled copper block.[1] Pellets were sliced into ~1 mm thick coins using a slow speed diamond saw with oil as a lubricant. Cut samples were then polished to a mirror finished using oil and 0.25 μm diamond lapping films. Extreme care was taken not to allow any contact between the specimens and water, due to the propensity of Mg-containing oxides to form hydrates. The resulting composite microstructure is shown in Fig. 1(a) (scanning electron microscope image obtained in backscatter mode to highlight the disparity in Z number between the Mg- and Hf-containing phases). The light regions in Fig. 1(a) correspond to the Hf-rich phase, while the dark regions correspond to the Mg-rich matrix phase. It can be seen from this micrograph that the synthesis route we employed resulted in a bimodal distribution of the Hf-rich phase dispersed within the Mg-rich matrix.

X-ray diffraction (XRD) measurements were made on the composite samples using a Bruker AXS D8 Advance X-ray diffractometer, Cu-K_α radiation, and θ–2θ geometry. A typical XRD pattern obtained from an as-synthesized, polished CERCER composite sample is shown in Fig. 1(b). Peak indexing of the XRD pattern was performed using Bruker AXS's Evaluation (EVA) program [12] combined with the Joint Committee for Powder Diffraction Studies database [13]. This analysis revealed that the as-fabricated microstructure consists of three phases: (1) cubic (c) MgO (JCPDF card # 045-0946 [14]) and a calculated lattice parameter of $a = 0.4208(2)$ nm; (2) rhombohedral (r) $Mg_2Hf_5O_{12}$ (JCPDF card # 033-0862 [15]) with calculated lattice parameters of $a = 0.942336$ nm and $c = 0.871813$ nm (hexagonal setting for the unit cell)[2]; and (3) a very small quantity of unreacted, monoclinic (m) HfO_2 (JCPDF card # 043-1017 [17]). This latter phase will be neglected for the remainder of this report. The phases produced via our synthesis route are predictable, based on the MgO–HfO_2 binary phase diagram published by Lopato et al. [18].

[1] We quenched from 1600 °C in a effort to retain a two-phase microstructure, consisting of nearly pure MgO and a cubic fluorite solid solution (F_{ss}) of hafnia and magnesia, as predicted in a phase diagram published by Wang et al. [11]. This phase diagram predicts that below 1500 °C, all MgO–HfO_2 compositions will phase separate into MgO and the monoclinic polymorph of HfO_2. Our intent was to avoid the monoclinic-HfO_2 phase.

[2] r-$Mg_2Hf_5O_{12}$ possesses rhombohedral (trigonal) symmetry and belongs to space group (S.G.) $R\bar{3}$ (No. 148 in the International Tables for Crystallography [16]). This structure is referred to in the literature as the delta (δ) phase and is associated with compounds consisting of stoichiometries near to M_7O_{12} (where M stands for a metal cation and O for an oxygen anion). Many M_7O_{12} compounds are known to crystallize in the δ crystal structure.

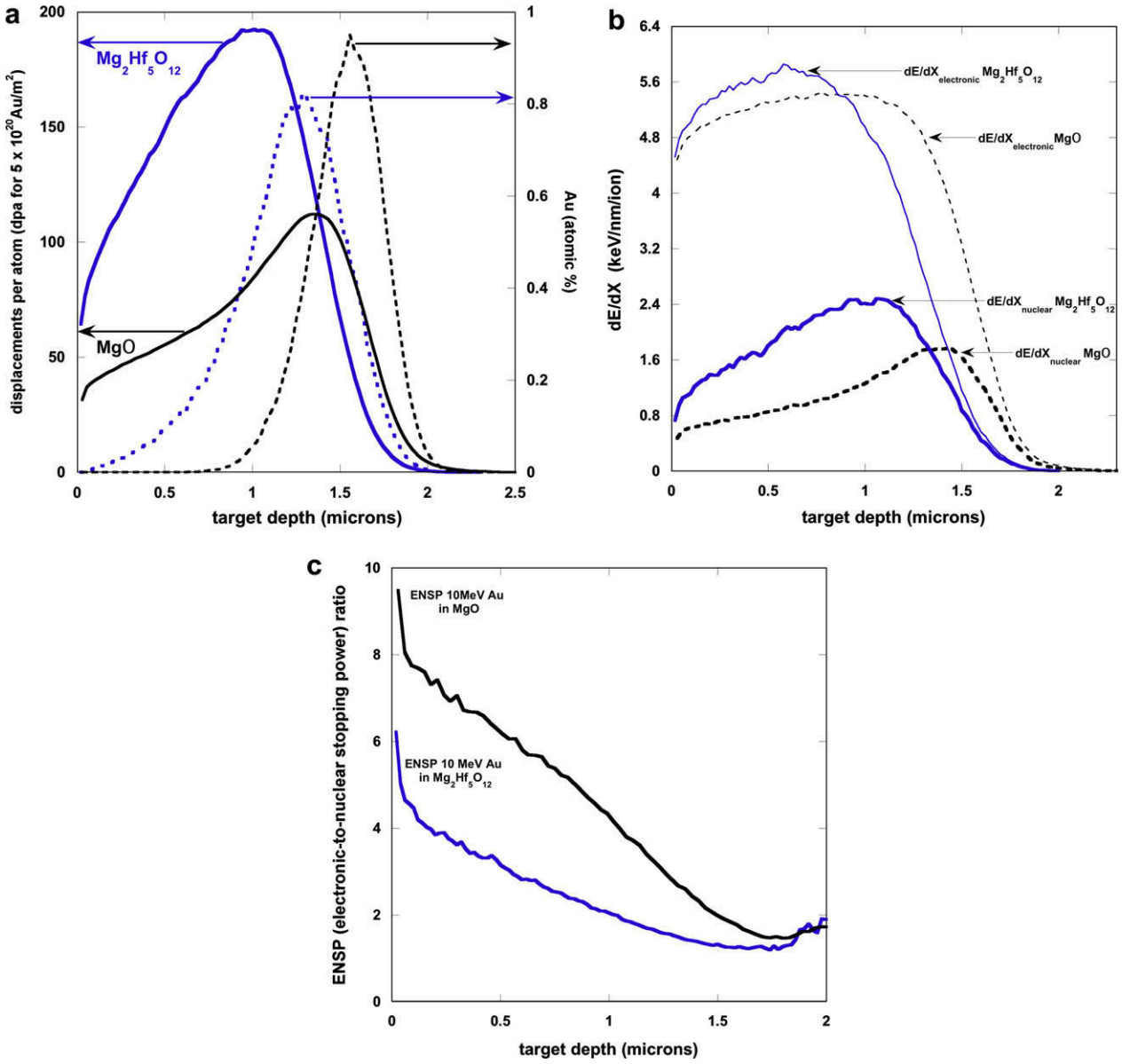

Fig. 2. (a) SRIM Monte-Carlo simulations for 10 MeV Au ion irradiations of MgO and $Mg_2Hf_5O_{12}$ (fluence = 5×10^{20} Au/m^2). The left-hand ordinate shows nuclear displacements in units of displacements per atom (dpa), as a function of target depth. The right hand ordinate shows the Au atomic concentration distribution within the separate targets. These curves reveal large differences in ballistic damage and ion penetration between MgO and $Mg_2Hf_5O_{12}$. (b) SRIM simulation estimates for nuclear and electronic energy loss as a function of depth for 10 MeV Au ion irradiations of MgO and $Mg_2Hf_5O_{12}$ (energy partitioning includes both primary and secondary recoil knock-on effects). (c) The electronic-to-nuclear stopping power (ENSP) ratio for 10 MeV Au ion irradiations of MgO and $Mg_2Hf_5O_{12}$ as a function of depth, based on the SRIM simulation results in (b). This plot indicates that the magnitude of ENSP in MgO is nearly twice that of $Mg_2Hf_5O_{12}$ over the first micron in either phase.

The as-fabricated, polished samples described above were irradiated using 10 MeV Au^{3+} ions at room temperature in the Ion Beam Materials Laboratory at Los Alamos National Laboratory, using a recently-developed medium energy ion irradiation set up on a 3.2 M.V. NEC Tandem accelerator supplied with an SNICS II ion source (setup fully-described in Ref. [19]). To assure irradiation uniformity, the scanning amplitude of the ion beam was set slightly larger than the dimensions defined by the pre-chamber slits. The standard irradiation area, which provided enough material for various post-irradiation characterization techniques, was set to 12×5 mm^2. Ion fluences ranged from 5×10^{16} to 5×10^{20} Au/m^2. Experimental results presented here will focus on the lowest and the highest fluences used in this study. In so doing, we will highlight our most important observations. All irradiations were performed at room temperature and using ion fluxes of 1×10^{14} and 4×10^{16} Au/m^2 $\times$ s in the 5×10^{16} and 5×10^{20} Au/m^2 ion-irradiated specimens, respectively.[3] Fig. 2(a–c) shows ion irradiation characteristics for 10 MeV Au^{3+} ion implantation into *c*-MgO and *r*-$Mg_2Hf_5O_{12}$, according to Monte-Carlo simulations using the ion transport code SRIM 2000 [20] (displacement energies of 40 eV for Hf, Mg and O atoms were used for these calculations; also, the densities of *c*-MgO and *r*-$Mg_2Hf_5O_{12}$, calculated from lattice parameters, were taken to be 3.59 and 8.48 g/cm^3, respectively). Fig. 2(a) shows estimates of ballistic damage (in units of displacements per atom or dpa) and implanted Au atomic

[3] The large differences between the fluxes used for the low and high fluence irradiations introduces the possibility for dose rate effects, which we did not examine in this study. However, without this flux change, the lowest fluence irradiation with the high flux would have required a time of just 1.2 s, while the highest fluence with the low flux would have required 58 days. Neither of these conditions is experimentally feasible.

concentration as a function of depth in *c*-MgO and *r*-$Mg_2Hf_5O_{12}$, for the highest fluence, 5×10^{20} Au/m^2, used in these experiments. It can be seen that a disparity exists not only in the 10 MeV Au ion penetration depth, but also in the peak damage dose, when comparing the pure *c*-MgO and *r*-$Mg_2Hf_5O_{12}$ phases. This disparity is due to the large difference in ion stopping power between MgO and $Mg_2Hf_5O_{12}$, which in turn, is due to the large molecular weight (M.W.) and atomic number (Z) differences between Mg (M.W. = 24.312 amu, $Z = 12$) and Hf (M.W. = 178.49 amu, $Z = 72$). Clearly, care must be used when analyzing and comparing ion specific irradiation damage effects in composite microstructures of varying Z numbers. Similar disparities are also found when comparing nuclear and electronic stopping powers between low- and high-Z composite phases. Fig. 2(b) shows estimates of energy loss partitioned between nuclear and electronic stopping for 10 MeV Au^{3+} ions as function of depth. Fig. 2(c) shows the electronic-to-nuclear stopping power (ENSP) ratio for 10 MeV Au^{3+} in both MgO and $Mg_2Hf_5O_{12}$ (based on Fig. 2(b) results). Plots in Fig. 2(b) and (c) include energy partitioning due to both primary knock-on atom (pk_a) and secondary knock-on recoil atom effects.

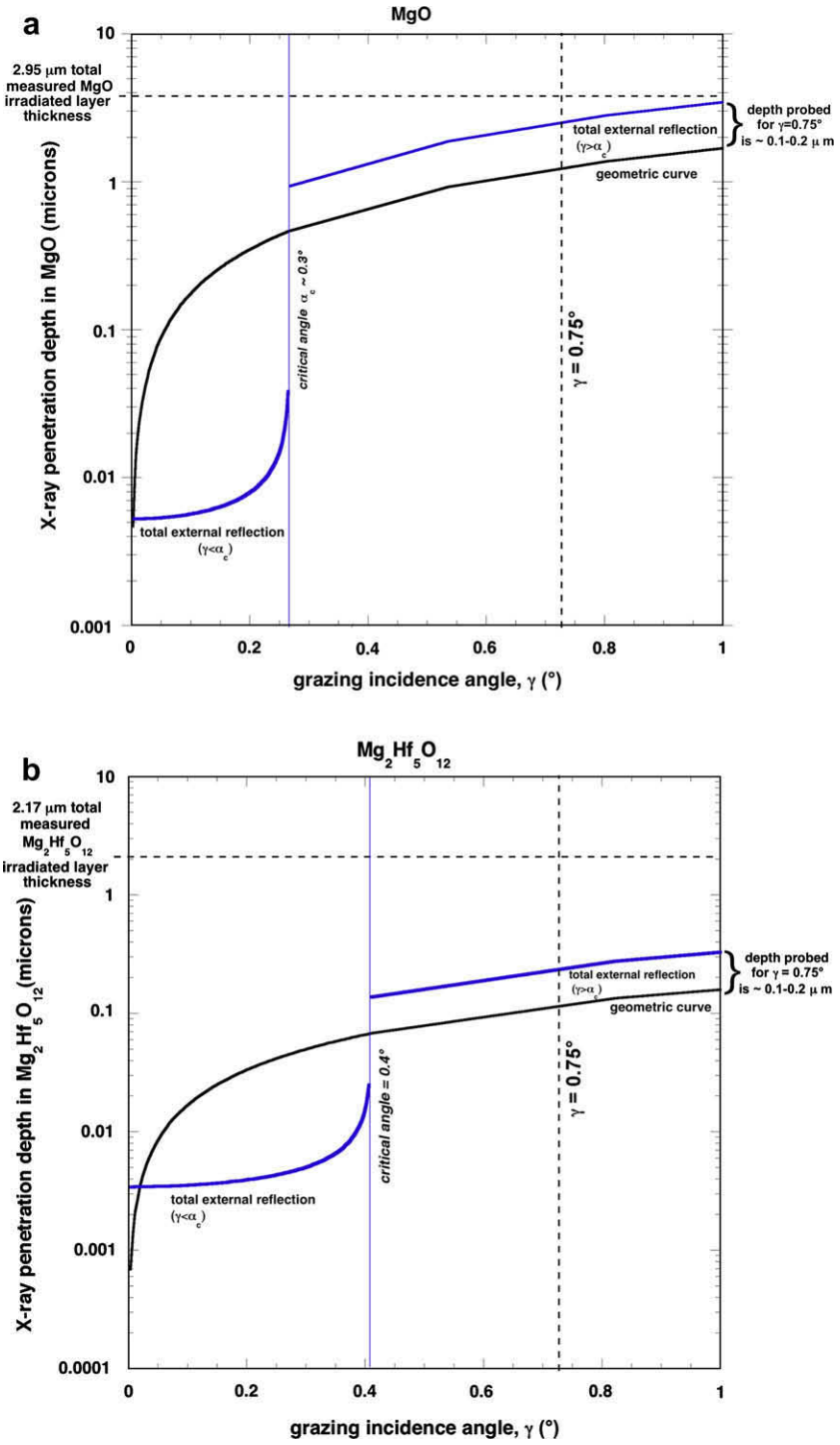

Fig. 3. Grazing incidence X-ray diffraction (GIXRD) X-ray penetration depth versus grazing incidence angle (γ) for (a) MgO and (b) $Mg_2Hf_5O_{12}$. Two methods for calculating X-ray penetration are shown in these plots (see text for discussion).

Ion irradiation damage was characterized using transmission electron microscopy (TEM) and grazing incidence XRD (GIXRD). Conventional TEM observations were made using a Philips CM-30 instrument operating at 300 kV. High-resolution TEM (HRTEM) observations were made using JOEL 3000F operating at (300 kV). GIXRD measurements were performed using a Bruker AXS D8 Advance X-ray diffractometer, Cu-K_α radiation, and θ–2θ geometry. The X-ray diffractometer was equipped with a Göebel mirror to achieve parallel beam diffraction optics. The θ–2θ scans were performed using a step size of 0.02° and a dwell time of 8 s per step, for scans over a 2θ range of 10–80°. GIXRD patterns presented in this study were obtained using a fixed incidence angle, $\gamma = 0.75°$. This angle was chosen based on material X-ray penetration calculations. Fig. 3 shows calculated penetration estimates for X-rays impinging on MgO and $Mg_2Hf_5O_{12}$ at varying grazing angles of incidence, g. X-ray penetration depths were estimated both geometrically (see, e.g., [21]) and based on critical angle (a_c), total external reflection theory (see, e.g., [22,23]). Geometrically, the GIXRD penetration depth is given by $\sin(\gamma)\sin(2\theta-\gamma)/\mu(\sin(\gamma)+\sin(2\theta-\gamma))$, where γ is the X-ray angle of incidence, 2θ is the diffraction angle for the particular measurement, and μ is the linear absorption coefficient ($\mu_{MgO} = 99.96\ cm^{-1}$ and $\mu_{Mg_2Hf_5O_{12}} = 1046\ cm^{-1}$ were calculated using Braggs additively law and specific mass absorption coefficients for Mg, Hf and O found in Ref. [24]). In terms of the critical angle for external reflection, a_c, the GIXRD penetration depth is given by $\lambda/2\pi(\alpha_c^2-\gamma^2)^{\frac{1}{2}}$ for $g < a_c$,

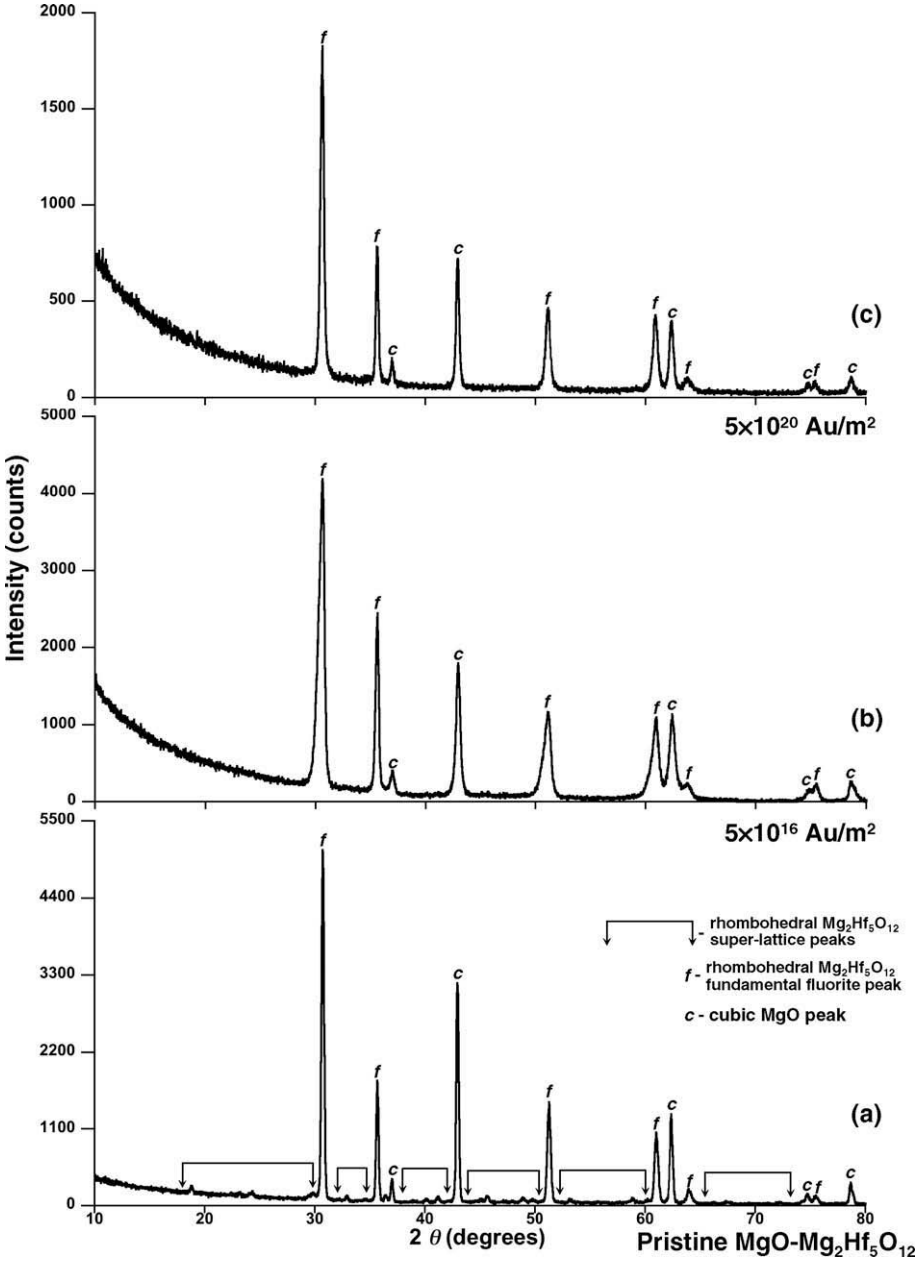

Fig. 4. GIXRD patterns (incidence angle $\gamma = 0.75°$) obtained from the following $90MgO{:}10HfO_2$ composite samples: (a) unirradiated; (b) irradiated with 10 MeV Au^{3+} ions to fluence 5×10^{16} Au/m^2; and (c) irradiated with 10 MeV Au^{3+} ions to fluence 5×10^{20} Au/m^2. Peak indexing of the GIXRD pattern in (b) revealed that an order–disorder (rhombohedral-to-cubic) transformation occurred in the second phase $Mg_2Hf_5O_{12}$ particles following ion irradiation to a fluence of 5×10^{16} Au/m^2. In the sample irradiated to the highest fluence performed in this study (5×10^{20} Au/m^2) the GIXRD pattern in (c) indicates that the ion-induced disordered phase (cubic-$Mg_2Hf_5O_{12}$) remains crystalline, even to this extreme ballistic damage dose of ~190 dpa. The MgO matrix phase also exhibited exceptional radiation stability, remaining in its original cubic form to a peak ballistic dose of ~120 dpa (pattern (c)).

and by $2\gamma/\mu$ for $g > a_c$, where λ is the X-ray wavelength and $\alpha_c \cong \sqrt{2\delta} = 1.6 \times 10^{-3}\sqrt{\rho}\lambda$, where $\delta = (1 - \eta)$ for refractive index, η (ρ is the density of the material in gm × cm^{-3} and λ is the X-ray wavelength in Å). The dotted lines overlaid on Fig. 3 shows the estimated depths probed using a grazing angle of incidence of $\gamma = 0.75°$. These calculations suggest that under these conditions, the depth probed in MgO is ~1–2 μm, while the depth probed in $Mg_2Hf_5O_{12}$ is ~0.1–0.2 μm. Since the peaks in the ion range distributions for MgO and $Mg_2Hf_5O_{12}$ are at ~1.6 and 1.3 μm, respectively (Fig. 2(a)), the calculated depth estimates above indicate that using $\gamma = 0.75°$, we probe primarily the ion-irradiated regions of our composite.

3. Results and discussion

Fig. 4 shows GIXRD patterns obtained from a pristine, polished composite sample and from composite samples irradiated to fluences of 5×10^{16} and 5×10^{20} Au/m^2. For the GIXRD pattern obtained from a pristine specimen, Bragg peaks labeled '*c*' belong to *c*-MgO, while all other Bragg peaks belong to the secondary phase, *r*-$Mg_2Hf_5O_{12}$ (these peaks include strong Bragg reflections labeled '*f*' which correspond to *r*-phase parent fluorite peaks, and numerous *r*-phase superlattice reflections (not individually labeled). It can be seen in the pattern corresponding to the specimen irradiated to the lowest fluence used in our study (Fig. 4(b), 5×10^{16} Au/m^2) that the superlattice reflections from the *r*-$Mg_2Hf_5O_{12}$ structure disappear, leaving only the fundamental fluorite diffraction maxima (labeled '*f*'). The '*f*' peaks correspond to a disordered disorder fluorite phase belonging to space group (S.G.) $Fm\bar{3}m$ (No. 225 in the International Tables for Crystallography [16]). In previous ion irradiation studies on various compounds with similar rhombohedral structures ($Sc_4Zr_3O_{12}$, $Lu_4Zr_3O_{12}$ and $Y_6W_1O_{12}$ [25–27]), we observed analogous order-to-disorder (*O*–*D*), rhombohedral-to-cubic (*r*–*c*) transformations (previous experiments used 300 keV Kr ions at cryogenic temperature). As for the *c*-MgO phase, no irradiation effects such as amorphization were observed. Also, there was no measurable change in the MgO cubic lattice parameter following irradiation. This result is consistent with previous ion irradiation damage studies on MgO performed by Matzke et al. [28–29].

The GIXRD pattern shown in Fig. 4(c) was obtained from the composite sample irradiated to the highest fluence used in these experiments (5×10^{20} Au/m^2). This fluence corresponds to peak displacement damage doses of 120 dpa in the MgO matrix and 190 dpa in the disordered *c*-$Mg_2Hf_5O_{12}$. Based on this GIXRD pattern, we conclude that the disordered *c*-$Mg_2Hf_5O_{12}$ phase persists with relatively little change, even to this extremely high ballistic dose of 190 dpa. GIXRD provided no indication of amorphization of the MgO or $Mg_2Hf_5O_{12}$ phases to ballistic doses of at least 120 and 190 dpa, respectively. We also observed peak broadening at both low and high ion fluences. This is usually associated with a decrease in grain size and or an increase in lattice strain. Interestingly, the peaks actually became sharper at the highest ion fluence. For instance, the fluorite (*f*) peak at 30.5° broadens by 120% (measured at full width half maximum) at low fluence (Fig. 4(b)), but only by 30% at high fluence (Fig. 4(c)), compared to the pristine sample peak width (Fig. 4(a)). At present, we have no good explanation for these changes (dose rate may play a role; recall that the dose rate for the sample in Fig. 4(b) is ~400 times smaller than for the sample in Fig. 4(c). Also X-ray peak intensities decreased while background increased, with increasing ion fluence. We believe this is due to an accumulation of lattice defects produced during irradiation as suggested by Makinson et al. [30] in their study of defects in nanocrystalline materials.

Fig. 5 shows a cross-sectional TEM image obtained from a composite sample irradiated with 10 MeV Au^{3+} ions to the highest fluence of 5×10^{20} Au/m^2 (~120–190 dpa). The TEM micrograph shows that the microstructure consists of light-contrast MgO grains and dark-contrast grains composed of $Mg_2Hf_5O_{12}$. This difference in contrast is due to the large difference in *Z* between the two materials. The selected-area electron diffraction (SAED) pattern obtained from the light-contrast MgO grain in the irradiated region (inset labeled, 'A' in Fig. 5) indexes as a rocksalt-type, cubic structure. Since pristine MgO is a rocksalt-like phase, this indicates that the MgO crystal structure is unaffected by the 10 MeV Au^{3+} ion irradiation. The micro-diffraction (μD) pattern obtained from the dark-contrast grain in the irradiated region (inset labeled 'B' in Fig. 5) indexes as a cubic, fluorite-type structure. This corroborates the GIXRD results in Fig. 4(c) and suggests that the $Mg_2Hf_5O_{12}$ has undergone an *O*–*D* (*r*–*c*) phase transformation due to ion irradia-

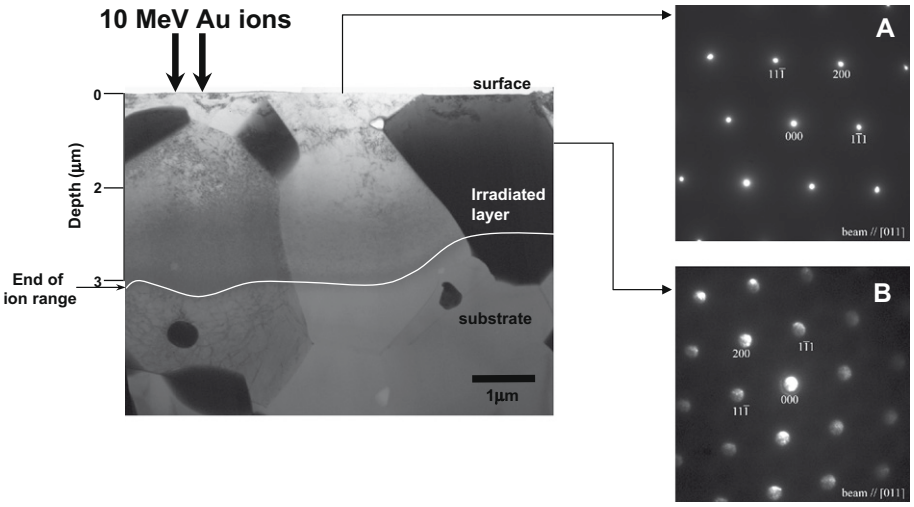

Fig. 5. Cross-sectional TEM micrograph obtained from a 10 MeV Au^{3+} ion-irradiated 90MgO:10HfO_2 specimen, irradiated to a fluence of 5×10^{20} Au/m^2. The micrograph reveals that both the MgO and $Mg_2Hf_5O_{12}$ phases remain crystalline to this high fluence, corresponding to peak ballistic damage doses of 120 and 190 dpa in the MgO and $Mg_2Hf_5O_{12}$ phases, respectively. Also shown in this micrograph is an undulating ion end-of-range, due to the vastly different ion stopping powers of MgO and $Mg_2Hf_5O_{12}$. The insets show electron diffraction patterns obtained from a light-contrast MgO grain (labeled A) and a dark-contrast $Mg_2Hf_5O_{12}$ grain (labeled B). Pattern A from the MgO grain indexes as a cubic, rocksalt-like structure, whereas the diffraction pattern labeled B indexes as a cubic, fluorite-like phase of $Mg_2Hf_5O_{12}$. Beam directions are labeled on the individual electron diffraction patterns.

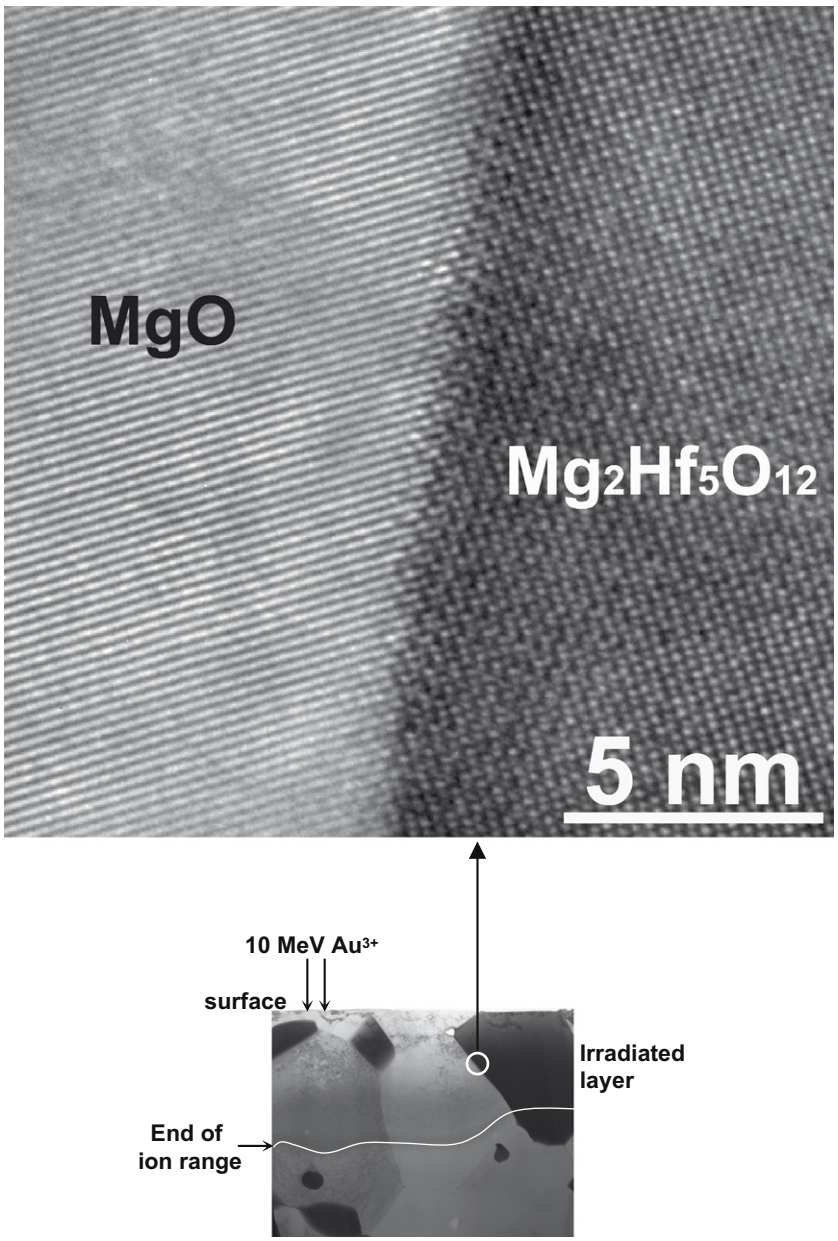

Fig. 6. HRTEM image obtained from an $MgO/Mg_2Hf_5O_{12}$ interfacial region (the circled region in the inset micrograph), following 10 MeV Au^{3+} ion irradiation to a fluence of 5×10^{20} Au/m^2. This image indicates that there is no sign of either intermixing at the inter-phase boundary or new phase formation.

tion. Lastly, Fig. 5 shows an interesting feature in that the Au ion end-of-range is observed to undulate in depth (white line trace in TEM image), instead of being a sharp interface between the irradiated and unirradiated regions. This result is not surprising in that mono-energetic ions (such as the 10 MeV Au^{3+} ions used in our experiments) must come to rest at different depths in a composite material, depending on the average *Z* of each phase encountered by the incident ions as they traverse the solid. It is also interesting to compare SRIM simulation results (Fig. 2) and TEM measurements (Fig. 5) regarding the range of 10 MeV Au in MgO and $Mg_2Hf_5O_{12}$. Apparently, SRIM underestimates the range of the Au ions by ~60% compared to TEM measurements. Currently, we do not have an explanation for this discrepancy.

Fig. 6 shows an HRTEM image obtained from an $MgO/Mg_2Hf_5O_{12}$ interface in a composite sample irradiated with 10 MeV Au ions to the highest ion fluence (5×10^{20} Au/m^2). The image shows a sharp phase boundary between the $Mg_2Hf_5O_{12}$ and MgO particles, with no signs of intermixing. This image suggests that for this particular composite system, excellent radiation stability can be expected at $MgO/Mg_2Hf_5O_{12}$ phase boundaries in high radiation environments, such as the radiation damage conditions experienced during service in a typical nuclear reactor core.

4. Conclusions

A CERCER polycrystalline composite synthesized from MgO and HfO_2 powders was ion-irradiated to assess its radiation stability. We observed an order-to-disorder (*O–D*) transformation (rhombohedral-to-cubic) in the $Mg_2Hf_5O_{12}$, high-*Z* component of this composite, by a fluence of 5×10^{16} Au/m^2. This fluence corresponds to a peak displacement damage dose of only ~0.02 dpa. This is a small ballistic dose, suggesting that the large electronic stopping power characteristic of 10 MeV Au ions (5.8 keV/nm peak) must play a significant role in the observed *O–D* transformation. This *O–D*

transformation was also accompanied by a decrease in density of the $Mg_2Hf_5O_{12}$. The MgO matrix phase showed no change to this fluence (based on GIXRD and TEM measurements). For the highest ion fluence used in our study (5×10^{20} Au/m^2), both the MgO matrix and the $Mg_2Hf_5O_{12}$ second phase exhibited no signs of amorphization or intermixing at phase boundaries.

Acknowledgements

This work was supported and sponsored by a Los Alamos National Laboratory, Laboratory Directed Research and Development (LDRD) Grant and by the US Department of Energy, Office of Basic Energy Sciences, Division of Materials Sciences and Engineering.

References

[1] Hj. Matzke, Radiat. Eff. 64 (1982) 3.
[2] L.W. Hobbs, F.W. Clinard, S.J. Zinkle, R.C. Ewing, J. Nucl. Mater. 216 (1994) 291.
[3] W.J. Weber, R.C. Ewing, C.R.A. Catlow, T. Diaz de la Rubia, L.W. Hobbs, C. Kinoshita, Hj. Matzke, A.T. Motta, M. Nastasi, E.K.H. Salje, E.R. Vance, S.J. Zinkle, J. Mater. Res. 13 (1998) 1434.
[4] K.E. Sickafus, L. Minervini, R.W. Grimes, J.A. Valdez, M. Ishimaru, F. Li, K.J. McClellan, T. Hartmann, Science 289 (2000) 748.
[5] D.R. Olander, Energy Research and Development Administration, Fundamental Aspects of Nuclear Reactor Fuel Elements, Technical Information Center, Office of Public Affairs, Springfield, Virginia, 1976.
[6] R.C. Ewing, W.J. Weber, J. Lian, J. Appl. Phys. 95 (2004) 5949.
[7] K.E. Sickafus, Hj. Matzke, T. Hartmann, K. Yasuda, J.A. Valdez, P. Chodak, M. Nastasi, R.A. Verrall, J. Nucl. Mater. 274 (1999) 66.
[8] H. Naguib, R. Kelly, Radiat. Eff. 25 (1975) 1.
[9] K.E. Sickafus, A.C. Larson, N. Yu, M. Nastasi, G.W. Hollenberg, F.A. Garner, R.C. Bradt, J. Nucl. Mater. 219 (1995) 128.
[10] J.A. Valdez, M. Tang, C. Zhenhuan, M.I. Peters, K.E. Sickafus, Nucl. Instrum. and Meth. B 218 (2004) 103.
[11] J. Wang, H.P. Li, R. Stevens, J. Mater. Sci. 27 (1992) 5397.
[12] Bruker Evaluation (EVA) Program, Version 13, Bruker AXS Inc., Madison, WI, USA, 2005.
[13] International Centre for Diffraction Data (1974 – present), Powder Diffraction File, Joint Committee on Powder Diffraction Standards, Philadelphia, PA.
[14] A. Kern, R. Doetzer, W. Eysel, Mineralogisch-Petrographisches Inst., Univ., Heidelberg, Germany, ICDD Grant-in-Aid, 1993.
[15] A. Garvish, Z. Inorg. Mater. (English Transl.) 14 (1978) 139.
[16] T. Hahn (Ed.), International Tables for X-ray Crystallography, vol. A, D. Riedel Publishing Co., Dordrecht, Netherlands, 1983.
[17] D. Grier, G. McCarthy, North Dakota State University, Fargo, North Dakota, USA, ICDD Grant-in-Aid, 1991.
[18] L.M. Lopato, A.V. Shevchenko, E.I. Zoz, G.I. Gerasimov, Neorg. Mater. 17 (1981) 90;
L.M. Lopato, A.V. Shevchenko, E.I. Zoz, G.I. Gerasimov, Inorg. Mater. (Engl. Transl.) 17 (1981) 66.
[19] I.O. Usov, J.A. Valdez, J. Won, M. Hawley, D.J. Devlin, R.M. Dickerson, B.P. Uberuaga, Y.Q. Wang, C.J. Olson Reichhardt, G.D. Jarvinen, K.E. Sickafus, Nucl. Instrum. and Meth. B 267 (11) (2009) 1918.
[20] J.F. Ziegler, J.P. Biersack, U. Littmark, in: J.F. Ziegler (Ed.), The Stopping and Range of Ions in Solids, Pergamon, New York, 1985.
[21] D. Rafaja, V. Valvoda, A. Vaclav, J. Perry, J.R. Treglio, Surf. Coat. Technol. 92 (1997) 135.
[22] A. Guinier, X-Ray Diffraction in Crystals, Imperfect Crystals and Amorphous Bodies, Dover Publications, Inc., New York, 1994.
[23] G. Lim, W. Parrish, C. Ortiz, M. Bellotto, M. Hart, J. Mater. Res. 2 (1987) 471.
[24] A.J.C. Wilson, E. Prince (Eds.), International Tables for X-ray Crystallography, vol. C, Kluwer Academic Publishers, Dordrecht, 1999.
[25] J.A. Valdez, M. Tang, K.E. Sickafus, Nucl. Instrum. and Meth. B 250 (2006) 148.
[26] K.E. Sickafus, R.W. Grimes, J.A. Valdez, A. Cleave, M. Tang, M. Ishimaru, S.M. Corish, C.R. Stanek, B.P. Uberuaga, Nat. Mater. 6 (2007) 217.
[27] M. Tang, J.A. Valdez, K.E. Sickafus, Nucl. Instrum. and Meth. B 376 (2) (2008) 247.
[28] Hj. Matzke, A. Turos, P. Rabette, O. Meyer, Solid State Phys. 14 (1981) 3333.
[29] Hj. Matzke, J.L. Whitton, Can. J. Phys. 44 (5) (1966) 995.
[30] J.D. Makinson, J.S. Lee, S.H. Magner, R.J. De Angelis, W.N. Weins, A.S. Hieronymus, Adv. X-ray Anal. 20 (1998) 407.